JOURNAL OF SOLID STATE CHEMISTRY 101, 48–58 (1992)

$YBa_2Fe_3O_8$ and the YCu(O)–BaCu(O)–YFe(O)–BaFe(O) Phase Diagram

P. KAREN, P. H. ANDRESEN, AND A. KJEKSHUS

Department of Chemistry, University of Oslo, Blindern, N-0315 Oslo 3, Norway

Received December 23, 1991; accepted April 9, 1992

Subsolidus phase relations are given under pseudo-isothermal conditions (910–950°C) for the YCu(O)–BaCu(O)–YFe(O)–BaFe(O) square section of the Y(O)–Ba(O)–Cu(O)–Fe(O) tetrahedral phase diagram. All samples are prepared from liquid-mixed citrate precursors, ensuring a relatively rapid establishment of equilibrium and high compositional resolution. A new phase, tetragonal $YBa_2Fe_3O_{8+w}$ ($w \approx 0.07$ when saturated in 1 atm oxygen), with $a = 391.67(3)$ and $c = 1181.78(12)$ pm, is synthesized and its stability limits toward the alternative formation of a disordered perovskite [$a = 399.58(5)$ pm] are given. A total of 8(1)% of the Fe atoms in $YBa_2Fe_3O_8$ can be replaced by Cu, which may be comparable to the situation for the $YBaCuFeO_5$ phase [13(5)%]. Up to 17(5)% of the Cu atoms in $YBaCuFeO_5$ can be replaced by Fe, as compared to 22(2)% for $YBa_2Cu_3O_7$ and some 20% for $BaCuO_2$. The existence of a large homogeneity envelope, originating at a perovskite-type $BaFe_{1-z}Y_zO_w$ phase with a z variable around 0.10 and $w \approx 2.6$, is found from mole-balance calculations of phase content. The homogeneity envelope comprises up to 20(5)% Cu for Fe substitution or up to 10(5)% Y for Ba substitution depending on the simultaneous presence of Y at the Fe site.

Introduction

Superconductivity occurs among selected oxides as a strictly element- and structure-specific phenomenon. Most of the oxide superconductors belong to the class of multicomponent oxocuprates and superconductivity has not been reported when other elements have replaced Cu in the structures concerned. Various transition metals can take over the Cu site in La_2CuO_4 (*1*), but none such crystal-chemical isotypes have so far been found for $YBa_2Cu_3O_7$. In this paper, we report on synthesis and chemical properties of such a variant, where Cu is completely replaced by Fe. The structure determination of the $YBa_2Fe_3O_8$ phase has been published separately (*2*); here we continue by locating $YBa_2Fe_3O_8$ within the framework of the YCu(O)–BaCu(O)–YFe(O)–BaFe(O) square section of the Y(O)–Ba(O)–Cu(O)–Fe(O) tetrahedral subsolidus phase diagram, which includes the structurally related phases $YBa_2Cu_3O_7$ and $YBaCuFeO_5$.

Experimental

Synthesis. The samples were synthesized using the technique of liquid mixing of citrate gels, followed by preparation cycles involving homogenization, firing, and controlled oxidation. Starting materials were Fe powder (3*N*+, Aldrich Chemical); Y_2O_3 (5*N*, Megon); $BaCO_3$ (reagent grade, Merck); $CuCO_3 \cdot Cu(OH)_2 \cdot 0.5H_2O$ (puriss, Riedel de Häen); and citric acid monohydrate (reagent grade, Fluka). Dried yttrium

0022-4596/92 $5.00

oxide was dissolved in melted citric acid monohydrate, and weighed amounts of dry $BaCO_3$ and analyzed basic copper carbonate were added to the solution. The desired amount of Fe was dissolved in a 1 : 1 aqueous solution of citric acid (5 mole of acid per 1 mole of Fe) upon oxidation to Fe^{3+} by gradual small additions of 10% H_2O_2. The resulting clear citrate gel was dehydrated at 180°C, incinerated at 450°C in air, and repeatedly fired at temperatures generally between 760 and 950°C, until phase purity and highest structural order were obtained according to powder X-ray diffraction (PXD). For the investigation of the phase compatibility diagram, the equilibration firings were limited to 910°C for samples with the Ba mole-content prevailing over that of Y, and to 950°C for the remaining portion of the system. When long annealings were still required to reach an equilibrium (exceeding some 100 hr), the pelletized samples were placed on a powder layer with the composition of the master sample to prevent direct contact with the corundum boat. The tube furnace used was flushed with oxygen gas purified on CuO at 600°C and on KOH at ambient temperature. The last rehomogenization cycle was appended by an oxygen saturation at 350°C for 16 hr.

Analysis of oxygen content. Oxygen content in samples which contained no Cu was determined gravimetrically by reduction in ultrapure hydrogen (≥ 99.99%, AGA Norgas) at 1000°C. A powdered sample of ~ 0.5 g, placed in a Pt boat, was reduced for 6 hr in H_2 (flow rate 250 ml/min). After cooling in a flow of ultrapure Ar (≥ 99.997%, AGA Norgas; flow rate 70 ml/min), the sample was immediately transferred into a dry atmosphere and weighed. The completness of the reduction into Fe and decomposition of $BaCO_3$ into BaO was checked by X-ray diffraction.

Oxygen content in samples which contained both Fe and Cu was determined iodometrically, upon masking Fe(III) by means of ammonium hydrogendifluoride in the presence of carbamide. The dissolution was carried out in a protective atmosphere of Ar and promoted by ultrasound agitation. Blank experiments were performed using corresponding amounts of $FeCl_3$ as a standard for Fe(III).

Analysis of carbon content. Samples were heated in flowing O_2 at 1100°C and the formed CO_2 was absorbed in a specified, excess amount of $Ba(OH)_2$. The remaining hydroxide was determined acidimetrically, using 0.1 M potassium hydrogenphtalate.

Powder X-ray diffraction. All samples were characterized by PXD measurements using Guinier–Hägg cameras, Cu$K\alpha_1$ radiation, and Si as an internal standard. High temperature PXD data were measured at temperatures between 300 and 1150 K using a Guinier–Simon camera (Enraf–Nonius) and Mo$K\alpha_1$ radiation. The samples, placed in a rotating quartz capillary open to the atmosphere, were heated at the rate of 50°C/hr. The thermometer was calibrated against the thermal expansion and melting point of Ag under the same conditions. Positions and integrated intensities of Bragg reflections were obtained from films by means of a Nicolet L18 film scanner using the SCANPI program system (*3*). The trial and error indexing was performed using the TREOR program (*4*). Unit cell parameters were deduced by least-squares refinements (*5*), including only unambiguously indexable lines. Quantitative estimates of the phase content were done based on comparisons of observed and calculated intensities, according to Fiala (*6*), using, however, only a few low angle PXD reflections, which were close enough (some 50 pm in terms of *d*-values) for the scattering volume dependence of the diffraction angle to be neglected, despite the beam transmission arrangement of the camera.

Results

In order to ensure that equilibrium is reached in those parts of the YCu(O)–BaCu

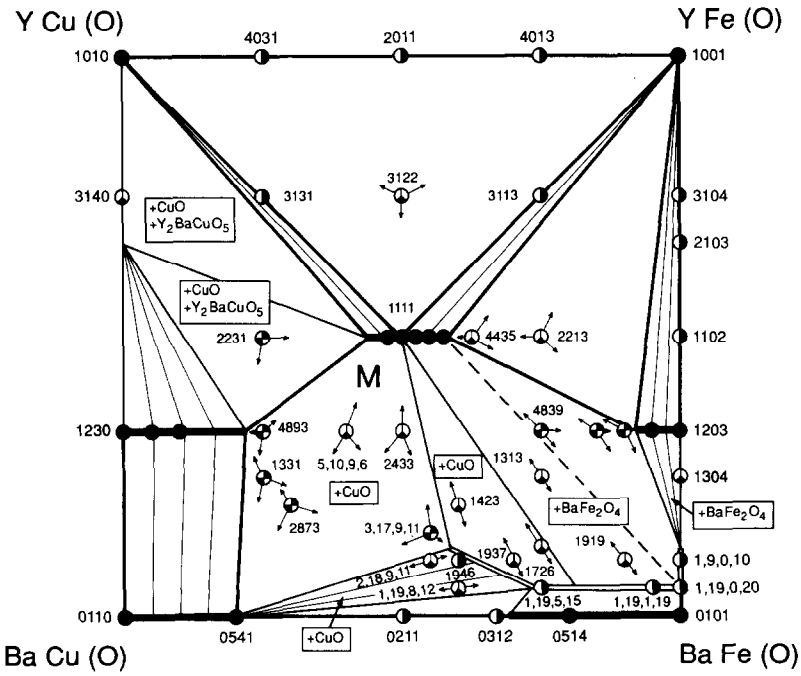

FIG. 1. Subsolidus phase compatibilities in the YCu(O)–BaCu(O)–YFe(O)–BaFe(O) system as seen by PXD at room temperature on samples equilibrated at 910°C for Y/Ba < 1 and 950°C for Y/Ba ≥ 1 and saturated in oxygen at 320°C. Nominal compositions are labeled by shorthand symbols for Y, Ba, Cu, and Fe, in the said sequence. The number of phases is indicated by partitioning of the circular symbols: (●) single phase, (◑) two phases, (◕) three phases, (●) four phases. Phase compositions are shown by arrows for phases within the plane and by labels for out-of-plane phases. Line distinctions: *very thin*, tie lines; *thin*, phase compatibilities out of the plane, as seen from the plane (location of broken such line is uncertain with respect to the Ba,Fe-rich endpoint); *medium*, phase compatibilities within the plane; *thick*, solid-solution ranges within the plane; *double thin*, solid-solution ranges out of the plane as seen from the plane. M represents an unresolved multiphase region where six phases were observed: Cu-rich 1111 solid solution; CuO (*Note*. Not seen in 5,10,9,6, and 2433 samples); Fe-sat 1230; Fe-sat barium cuprate ($a \approx 1838$ pm, for samples 1331 and 2874); Fe-sat barium cuprate ($a \approx 1842$ pm); and Cu-sat $Ba(Cu,Fe,Y)O_3$ (cubic perovskite).

(O)–YFe(O)–BaFe(O) system which have high liquidus temperatures and, on the other hand, to avoid the appearance of liquidus in other parts of the diagram where it would significantly decrease the compositional resolution, the study was not carried out under strictly isothermal conditions. The subsolidus phase relations in the YCu(O)–BaCu (O)–YFe(O)–BaFe(O) system are depicted in Fig. 1, referring to the situation at 910°C for Y/Ba < 1 and 950°C for Y/Ba ≥ 1 with subsequent slow cooling and a 16-hr saturation in oxygen at 350°C. Apart from the multiphase area marked M, Fig. 1 represents an approximate phase diagram. An idea regarding how M may resolve into phase compatibility regions will be considered later.

The occurrence and orientation of the extended solid-solution ranges in this system indicate a certain degree of chemical similarity between the components—most pronounced between Cu and Fe. However, as a likely consequence of the difference in the valence stability between these elements,

negligible solid solubility is observed for the stoichiometric compounds $Y_2Cu_2O_5$ and $YFeO_3$, where the atoms concerned take only one valence state. The deduction is based on judgments of unit cell volumes in relation to the nominal sample composition: For $YFeO_3$, $V = 224.70(3) \times 10^6$ and $224.57(2) \times 10^6$ pm^3, respectively, are found for samples with nominal compositions 2011 and 4013, as compared to $V = 224.70(5) \times 10^6$ pm^3 for the pure phase.[1] Similarly, for $Y_2Cu_2O_5$, $V = 470.09(8) \times 10^6$ pm^3 is found in the 4031 two-phase sample, as compared to $V = 470.32(6) \times 10^6$ pm^3 for the pure phase. Apart from these just mentioned oxides, four solid-solution regimes originating from ternary or quaternary oxides (edges or corners of the phase diagram) are observed, and are described in the following.

(i) The $YBa_2(Cu_{1-z}Fe_z)_3O_{6.95+1.05z}$ (1230) solid solution extends to $z = 0.22(2)$, according to the mole-balance estimates from the phase content of the nominal 4893 sample (corresponding to $z = 0.25$). The analyzed oxygen contents indicate that the formal Cu valency remains constant when z varies [next to Fe(III)] as expressed by the above formula. The unit cell parameters versus z relationships [Fig. 2; for high temperature data see Ref. (*7*)] correspond to the oxidative regime during the syntheses (*8*), when Fe atoms are hypothesized (*9*) to have a tendency for locating themselves along the twin boundaries, thus in turn diminishing the domain size and favoring the (apparent) transition from orthorhombic to tetragonal structure. The variation of unit cell volume with z reflects the larger atomic size of Fe as compared to Cu.

(ii) The $YBa_2(Fe_{1-z}Cu_z)_3O_8$ (1203) solid solution extends to $z = 0.08(1)$, according to the variation in the unit cell data with

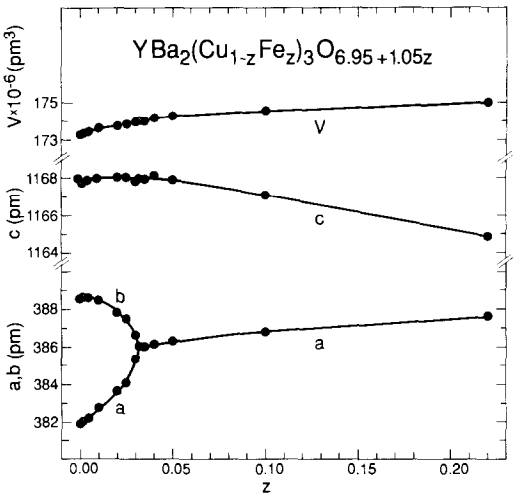

FIG. 2. Unit cell data at 300 K as functions of Fe for Cu substitution in $YBa_2(Cu_{1-z}Fe_z)_3O_{6.95+1.05z}$. Size of the symbols is at least five times the standard error.

nominal z (Fig. 3). This solid-solubility limit must be characterized as surprisingly low, considering the pronounced similarity of the $YBa_2Fe_3O_8$ triple-perovskite structure to that of $YBa_2Cu_3O_7$. The only significant structural difference stems from the higher

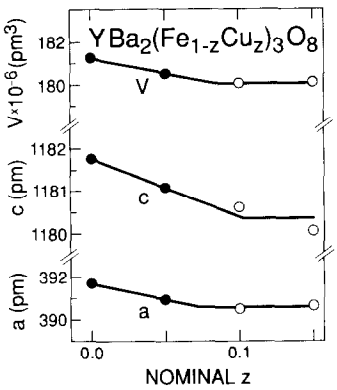

FIG. 3. Unit cell data of $YBa_2(Fe_{1-z}Cu_z)_3O_8$ at 300 K as functions of nominal z. Closed circles refer to single-phase, open circles to multiphase products. Size of the symbols is at least five times the standard error. Weight has been put on V in the assessment of phase limit [0.08(1)].

[1] Shorthand symbols of the type 1203, as for $YBa_2Fe_3O_8$, are used throughout the paper when the relative proportions of the metal atoms rather than the complete formulae are of importance.

oxygen content of the Fe variant, complementing the coordination squares to octahedra, leading to a tetragonal symmetry and a slight increase in the unit cell parameters [to $a = 391.67(3)$ and $c = 1181.78(12)$ pm]. Since the content of the residual carbon, 0.03 wt% C, corresponds to the analytical background (observed for the analogous cuprate), the used hydrogen-reduction method for analysis of oxygen content refers solely to oxygen, giving 8.06 oxygens per formula unit. Because this method tends to give slightly higher-than-correct oxygen contents for the analogous cuprate, the analyses were also performed by iodometry. However, the slight nonstoichiometry was confirmed, and an oxygen content of 8.07(1) was obtained for the oxygen-saturated sample. When Cu substitutes a portion of Fe, the extra oxygens are practically absent, and, e.g., a composition $YBa_2(Fe_{0.95}Cu_{0.05})_3O_{8.01(1)}$ is obtained for a phase-pure, 5% solid-solution sample. High temperature Guinier–Simon photographs of the $YBa_2Fe_3O_{8.07(1)}$ powder samples revealed the absence of any structural transitions up to 1150 K. The thermal expansion is almost linear in a, c, and V and the expansion coefficients are $\alpha_a = 1/a \cdot \Delta a/\Delta T = 15.9(4) \times 10^{-6}\,K^{-1}$; $\alpha_c = 21.3(4) \times 10^{-6}\,K^{-1}$ and $\alpha_V = 54(1) \times 10^{-6}\,K^{-1}$.

The formation of $YBa_2Fe_3O_8$ was investigated within a wide temperature range of 760–1200°C. While this triple perovskite is readily formed at, say, 950°C a disordered, single perovskite appears at low temperatures (around 800°C)—nota bene, all results referring to the liquid-mixed citrate precursor technique. Due to the fine dispersion of the submicrometer incineration product, consisting of Y and Fe oxides and Ba carbonate, the cubic $Ba_{2/3}Y_{1/3}FeO_{2.7}$ [$a = 399.58(5)$ pm] is obtained in a pure state apart from (usually) some of the ordered phase, after just a few cycles of firings in CO_2-free oxygen. Observed and calculated PXD data for this low temperature, single-perovskite phase are listed in Table I. Once formed, the single-perovskite phase is subject to only a relatively slow ordering process, requiring some 300 hr at, say, 900°C for the cubic phase to disappear and an additional ~700 hr to obtain a complete, well-developed, PXD pattern for the triple perovskite $YBa_2Fe_3O_8$. A contraction to 95% of the molar volume of the low temperature disordered solid occurs as a consequence (or perhaps rather as a cause) of the ordering. To establish whether the low temperature, disordered phase is stabilized kinetically or thermodynamically requires a further detailed investigation. However, the kinetic alternative seems most feasible since the solid state diffusion rate for the larger cationic elements (Y and Ba) can be considered low at low temperatures. Hence, the random distribution already established in the liquid-mixed precursor would tend to be preserved for Y and Ba, while the higher diffusion rate for Fe and oxygen could allow for their ordering into the perovskite structure. Such low-temperature formation of a metastable solid solution has been observed, e.g., in the Sc_2O_3–Mn_2O_3 system (*10*).

Also the high temperature stability of the ordered $YBa_2Fe_3O_8$ phase is rather limited, and, above some 1100°C, the presence of a

TABLE I

PXD DATA FOR $(Y_{1/3}Ba_{2/3})FeO_{2.7}$, Space Group $Pm\bar{3}m$

d_o (pm)	hkl	$(I/I_0)_o$	$(I/I_0)_c$
399.2	100	8	9
282.5	110	100	100
230.5	111	13	16
200.3	200	50	35
—	210	—	5
163.2	211	29	44
141.2	220	5	25
—	300; 221	—	1
126.4	310	4	25

cubic perovskite [a = 407.6(5)] and Ba Fe_2O_4 is apparent after a few hours annealing in oxygen. After a quick melting of $YBa_2Fe_3O_8$ in an alumina crucible, a cubic, spinel-like phase with a = 870.21(7) pm is predominant in the quenched melt, but there were clear marks of reaction between the sample and the crucible, and this line was not pursued further.

At this point, the present authors also like to record that they have tried to prepare $YBa_2M_3O_w$ with M = Mn, Co, and Ni. A variety of preparation routes, oxygen pressures, temperatures, and heating periods have been tested, but all attempts have so far been in vain.

(iii) The $Ba(Cu_{1-z}Fe_z)O_{2+w}$ (0110) solid solution extends to $z \approx 0.2$, as can be judged from the unit cell parameter a versus nominal z plot in the upper part of Fig. 4. This solid-solubility limit is comparable to that for the neighboring $YBa_2Cu_3O_7$ phase. However, contrary to the latter phase, an increase in the Cu formal valency next to Fe(III) is found iodometrically for increasing z. The oxygen content increases rapidly with z, and w = 0.11 is found for z = 0 [a = 1830.9(6) pm], w = 0.23 for z = 0.2 [a = 1838(2) pm].

(iv) The $Ba(Fe_{1-z}Cu_z)O_{3-w}$ (0101) solid solution extends to $z \approx 0.3$, according to the variation in the unit cell data with nominal z, shown in the lower part of Fig. 4. This solid-solubility limit is rather high (cf. Fig. 1), and another puzzling feature is associated with the fact that the unit cell parameters increase with increasing substitution of Cu for Fe. According to the iodometric determinations, the oxygen content could provide a clue, since while the content of 2.90(1) oxygens per formula is found for z = 0, a significantly lower value of 2.80(1) is found for z = 0.2, and 2.70(1) at the solid-solubility limit.

There occurs only one genuine quintenary oxide phase in the YCu(O)–BaCu(O)–YFe(O)–BaFe(O) system, the $YBaCu_{1-z}Fe_{1+z}O_5$ solid solution, derived from the

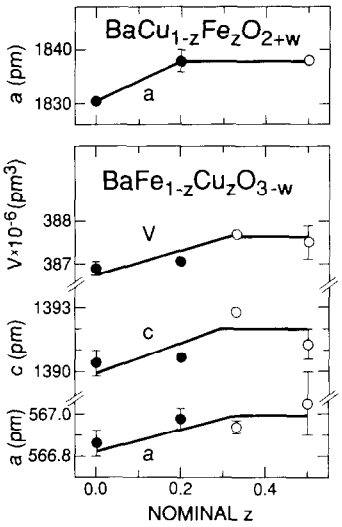

FIG. 4. Unit cell data at 300 K as functions of z in samples with the nominal compositions $Ba(Cu_{1-z}Fe_z)O_{2+w}$ (upper) and $Ba(Fe_{1-z}Cu_z)O_{3-w}$ (lower). Closed circles refer to single-phase, open circles to multiphase products. Size of the symbols corresponds to the standard error or it is indicated by error bars. Weight has been put on V in the assessment of the phase limit for $Ba(Fe_{1-z}Cu_z)O_{3-w}$ [0.30(2)].

$YBaCuFeO_5$ structure with two different, Cu- and Fe-centered, square-pyramidal coordinations, open for respectively Fe and Cu substitution. As a consequence of this, the range of solid solubility extends toward both Cu and Fe, and, because of the difference between the substituents, the unit cell parameters as functions of z exhibit kinks at z = 0. However, the unit cell volume varies reasonably smoothly across z = 0. Apparently due to these features, the estimate of the solid-solubility limits from the cell data gives results contradicting the observed phase composition (Fig. 5), and only the lower limit can be obtained reliably, z = −0.13(5). When the upper limit is derived by the mole-balance considerations from the phase content of the sample 4435 [with nominal z = 0.25 and the following content in pseudoatom %: $YBaCu_{1-z}Fe_{1+z}O_5$, 83%; $YBa_2(Fe_{0.92}Cu_{0.08})_3O_8$, 11%; $YFeO_3$, 6%] a

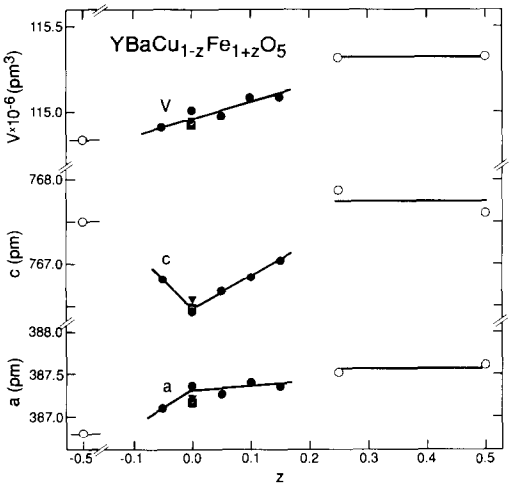

FIG. 5. Unit cell data at 300 K as functions of z in samples with the nominal composition $YBaCu_{1-z}Fe_{1+z}O_5$. Closed circles refer to single-phase, open circles to multiphase products. The standard error does not exceed the size of the symbols. For assessment of phase limits see text.

limit of $z = 0.12(7)$ is obtained, the estimated error referring to an arbitrary 50% error in the content of the minor phases. Combined with the phase-purity observations indicated in Fig. 5, the overall upper solid-solubility limit for $YBaCu_{1-z}Fe_{1+z}O_5$ is assessed at $z = 0.17(5)$. (Note that minor amounts of impurity phases in the nominal $z = 0.15$ sample could easily have remained undetected.)

The extents of the solid solubility of Fe at the Cu site and Cu at the Fe site are close to the respective substitution limits for the neighboring phases 1230, 0110, and 1203 (see Fig. 1) Limited oxygen content variation was found in the investigated portion of the solid-solution range which implies that the oxidation states associated with the Fe and Cu sites must be carried over to the substituents.

Due to its central location, the $YBaCu_{1-z}Fe_{1+z}O_5$ solid-solution phase coexists with most of the other phases in the system (notably not with the 0101-based solid solution). The actual compositions of the $YBaCu_{1-z}Fe_{1+z}O_5$ solid solution which are in equilibrium with the other phases have been judged from the unit cell data for this phase in the appropriate multiphase mixtures, and a very consistent picture is obtained for various multiphase samples. The results are indicated in Fig. 1 by the direction of the arrows (note also the symbol distinctions).

The composition of the multiphase samples in the Ba- and Fe-rich portion of the YCu(O)–BaCu(O)–YFe(O)–BaFe(O) system in Fig. 1 is dominated by a cubic solid-solution phase with unit cell parameters a ranging between ~401 and ~407 pm. The systematic extinctions in the PXD pattern indicate a primitive cell and the distribution of intensities in the pattern corresponds to a perovskite-type structure based on the composition $BaFeO_{3-w}$. This phase never occurs phase pure in the YCu(O)–BaCu(O)–YFe(O)–BaFe(O) square section of the tetrahedral system, and the appearance of CuO in the Cu-richer portion and of $BaFe_2O_4$ in the Cu-poorer portion suggests that the phase is located "above" the plane which constitutes Fig. 1; i.e., it has higher Ba content. The distance from the plane apparently varies, and a nearly pure cubic perovskite occurs at the 1,19,0,20 composition. Including the iodometrically determined oxygen content, the composition of the sample corresponds approximately to $(Ba_{0.95}Y_{0.05})FeO_{2.81(3)}$. The observed and calculated PXD data for this composition and an assumed perovskite-type arrangement are listed in Table II, and the relative good fit encouraged us to use the calculated diagram for estimations of phase contents. Supplementary crystal structure data for $YBaCuFeO_5$ (*11*), $YBa_2Fe_3O_8$ (*2*), hexagonal (6H) $BaFeO_{2.73}$ (*12*), $BaFe_2O_4$ (*13*), CuO (*14*), $BaCuO_2$ (*15*), and $YBa_2(Cu_{0.9}Fe_{0.1})_3O_{7.1}$ (*16*) were utilized, and the actually observed unit cell parameters were used in these calculations.

In the YFe(O)–BaFe(O) range, this ap-

TABLE II

PXD DATA FOR $(Ba_{0.95}Y_{0.05})FeO_{2.81}$, Space Group $Pm\bar{3}m$

d_o (pm)	hkl	$(I/I_0)_o$	$(I/I_0)_c$
402.06	100	17	20
284.23	110	100	100
231.97	111	26	22
200.94	200	41	33
179.69	210	11	11
164.03	211	55	44
142.04	220	24	24
133.95	300; 221	4	7
127.05	310	21	25
121.09	311	7	12
115.96	222	6	11

proach led to relatively precise results for the composition of the cubic phase, since the phases involved are close to the cubic phase in composition and occur in low content. Thus, even large errors in the quantitative estimate are transferred into a minor deviation in the composition of the main phase. The results of the phase analyses and of the following mole-balance estimates for the composition of the cubic perovskite $(Ba,Y)(Fe,Y)O_{3-w}$ are listed in Table III.

The estimates of the composition of the cubic phase became generally less accurate when the Cu content also entered the balances. Nevertheless, multiphase samples adjacent to the most Cu-rich region with the cubic phase as the main component almost invariably gave a composition, expressed by the formula $Ba(Cu_{0.2}Fe_{0.8-z}Y_z)O_{3-w}$, $z \in (0.06; 0.15)$, $w \in (0.36; 0.38)$, i.e., with a practically constant Cu content and a Ba content which matches the sum of Cu, Fe, and Y. The said compositions are located in a triangle erected from the BaCu(O)–BaFe(O) line toward the BaY(O) point of the tetrahedral phase diagram, and their projection onto the YCu(O)–BaCu(O)–YFe(O)–BaFe(O) plane, with CuO in the focal point, would indeed account for the kink on the two-phase line in Fig. 1 (traced as double) as being a consequence of the Cu saturation of the cubic phase. Recently, the formation of a Y-stabilized, cubic perovskite phase $Ba(Fe_{0.9}Y_{0.1})O_{2.59}$ has been described by Parras *et al.* (*17*), and this supports the inference that the presently observed cubic phase is actually a Ba $(Fe_{1-z}Y_z)O_{3-w}$ solid-solution phase where up to some 20% of the Fe sites can be substituted by Cu, or up to some 10% of Ba can be replaced by Y, when the Y concentration at the Fe site is harmonized. The resulting situation is depicted in Fig. 6, within the complete frame of the tetrahedral phase diagram.

The inferrence is that the homogeneity envelope of the cubic phase has a wedge shape, whose sharp edge, together with one of the four long edges and one of the short edges, is a border of multiphase regions intersecting the square plane; i.e., their compositions are "seen" in the appropriate mul-

TABLE III

COMPOSITIONS OF THE CUBIC $(Ba_{1-y}Y_y)(Fe_{1-z}Y_z)O_{3-w}$ PHASE IN NOMINAL YFe(O)–BaFe(O) SAMPLES, AS OBTAINED BY PXD

	Phase content (pseudo-atom fractions)				Phase D		
Sample	A	B	C	D	y	z	a (pm)
1,19,0,20	0.10	0.01	—	0.89	0.055	~ 0	401.7(4)
1,9,0,10	—	0.12	—	0.88	0.07	0.04	402.3(1)
1304	—	0.03	0.8	0.17	0.1	0.1	403.0(4)

Note. A, $BaFeO_{2.73}$; B, $BaFe_2O_4$; C, $YBa_2Fe_3O_8$; D, $(Ba_{1-y}Y_y)(Fe_{1-z}Y_z)O_{3-w}$ (cubic phase).

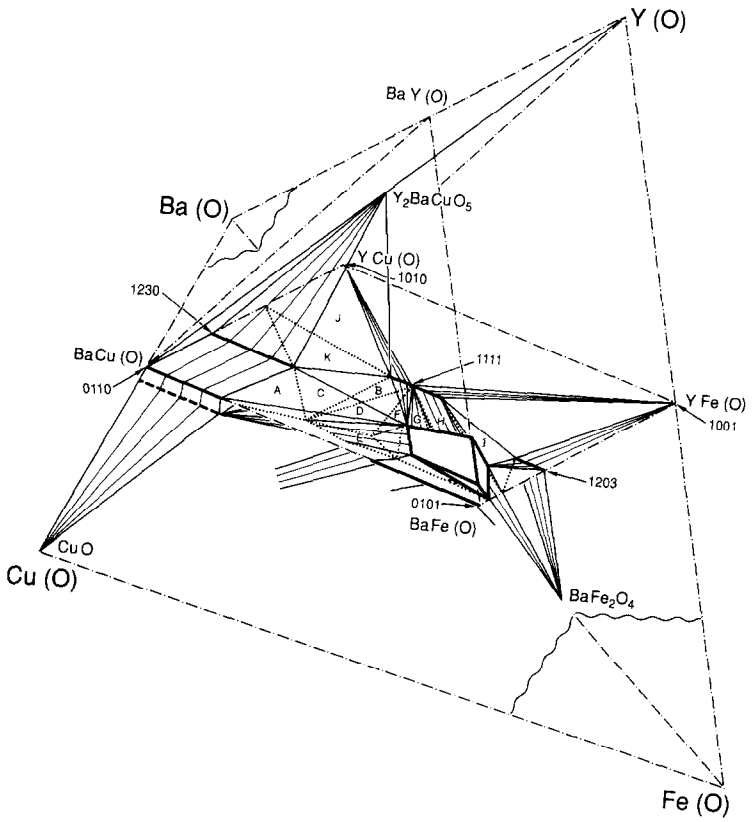

FIG. 6. Location of phases observed outside the YCu(O)–BaCu(O)–YFe(O)–BaFe(O) square section of the Y(O)–Ba(O)–Cu(O)–Fe(O) tetrahedral phase diagram. Line distinctions: *chain*, frame of diagram and auxiliary planes; *thin*, tie lines; *medium*, phase compatibility lines; *thick*, solid solutions. Notations for phase fields (sat, saturated; s.s., solid solution): A, Fe-sat 1230 | Fe-sat $BaCuO_2$ | Fe-sat $BaCu_{1+x}O_2$ | Cu,Y-sat $Ba(Cu,Fe,Y)O_3$; B, Cu-rich 1111 s.s. | Fe,Cu-sat $BaCu_{1+x}O_2$ | Cu,Y-sat $Ba(Cu,Fe,Y)O_3$; C, Fe-sat 1230 | Cu-sat 1111 | Fe,Cu-sat $BaCu_{1+x}O_2$ | Cu,Y-sat $Ba(Cu,Fe,Y)O_3$; D, 1111 | Fe,Cu-sat $BaCu_{1+x}O_2$ | Cu,Y-sat $Ba(Cu,Fe,Y)O_3$ | CuO; E, Fe,Cu-sat $BaCu_{1+x}O_2$ | Cu-sat $Ba(Cu,Fe,Y)O_3$ s.s. | CuO; F, 1111 | Cu-sat $Ba(Cu,Fe,Y)O_3$ s.s. | CuO; G, 1111 | Y-poor,Cu-rich $(Ba,Y)(Cu,Fe,Y)O_3$ s.s. | CuO; H, Fe-rich 1111 s.s. | Y-poor,Cu-poor $(Ba,Y)(Cu,Fe,Y)O_3$ s.s. | $BaFe_2O_4$ type; I, Fe-sat 1111 | Cu-sat 1203 | Y-sat $(Ba,Y)(Fe,Y)O_3$; J, Cu-sat 1111 | $Y_2Cu_2O_5$ | Y_2BaCuO_5 | CuO; K, Fe-sat 1230 | Cu-sat 1111 | Y_2BaCuO_5 | CuO.

tiphase samples included in Fig. 1. The unit cell parameters of the cubic phase as observed in various samples are listed in Table IV, and these findings comply with the presumed continuous character of the cubic solid-solution region; a increasing with decreasing Y for Ba substitution and increasing Y for Fe substitution.

The division of the adjacent Cu-richer and -poorer portions in the square plane into the appropriate multiphase regions, which is unresolved in Fig. 1, could now be attempted. The separation of the H and I regions in Fig. 6, between the samples 4839 and 1313, is possible only when the Fe solid solubility in the 1111 phase is not higher than some 15%, which corresponds to the mole-balance estimate from the phase content of

TABLE IV

UNIT CELL PARAMETERS OF CUBIC $(Ba_{1-y}Y_y)(Fe_{1-z'-z''}Y_{z'}Cu_{z''})O_{3-w}$ IN MULTIPHASE SAMPLES FROM THE YCu(O)–BaCu(O)–YFe(O)–BaFe(O) SYSTEM

Sample	a (pm)	Sample	a (pm)	Sample	a (pm)	Sample	a (pm)
20,40,9,51	402.7(2)	1,19,1,19	401.3(3)	1,19,8,12	403.1(2)	3,17,9,11	405.8(1)
4839	402.1(8)	1726	401.2(1)	1423	403.6(1)	2433	407.3(2)
1313	400.9(1)	1,19,5,15	401.3(2)	1946	403.9(2)	5,10,9,6	408.4(3)
1919	400.6(1)	1937	403.5(1)	2,18,9,11	404.9(1)	2873	406.7(4)

the sample 4435 [12(7)]. However, a significant Cu solid solubility in the $BaFe_2O_4$ phase could change the picture. In the area delimited by the saturated solid solutions based on 1111, 1230, 0110, and the cubic phase, the compositions of the samples indicate that a subdivision into (a few) smaller regions occurs, which could be accomplished only by assuming that the $BaCuO_2$-type (0110) solid solution has another compositional or homogeneity dimension, toward Cu, according to the formula $Ba(Cu_{1-z}Fe_z)_{1+x}O_{2+w}$. The implied metal excess for the $BaCuO_2$-based phase would be permitted by the structure model in Ref. (*15*) and follows also from some studies of the Ba(O)–Cu(O) system (*18, 19*). On the other hand, no solubility for Y at the Ba site is found to occur (*20*). Additional support stems from the fact that the iron-saturated $BaCuO_2$ phase, when located strictly in the BaCu(O)–BaFe(O) system, has unit cell parameter a = 1838(1) pm, whereas, when seen from the CuO containing parts of the square plane, an invariably larger cell with a = 1841 to 1842 pm is observed (samples 5,10,9,6; 2433; 2,18,9,11; 1,19,8,12). In the region close to the iron-saturated 0110 phase, the unit cell parameter diminishes, and a = 1839(2) is found for 1331 and a = 1838(2) pm for 2873. Finally, a definite proof has been obtained by preparation of a sample with a below-the-plane location. An attempted overall $BaCu_{0.85}Fe_{0.20}O_{2.27(1)}$ composition (oxygen content in the bulk product by iodometry) consisted of two closely related phases, viz., the regular, $BaCuO_2$-based solid solution $Ba(Cu_{0.85}Fe_{0.15})O_{\sim 2.2}$ (one-third of the sample), with a = 1836(2) pm, and the excess-metal solid-solution $Ba Cu_{0.85}Fe_{0.226}O_{\sim 2.4}$ (two-thirds of the sample), with a = 1841.2(5), according to mole-balance estimates from phase content, oxygen content analyses, and data in Fig. 4. PXD shows that the structures of these phases are clearly derived from $BaCuO_2$, and their occurrence could therefore deserve further study.

In this region, the YCu(O)–BaCu(O)–YFe(O)–BaFe(O) plane then intersects several three- and four-phase tetrahedral envelopes (where one edge must be a solid solution in the former case) as indicated tentatively in Fig. 6. The closeness of these envelopes, which suggests very similar ΔG levels for the involved phases, would also provide an explanation for the very slow approach to equilibrium in some parts of the investigated area.

Concluding Remarks

A square section of the tetrahedral phase diagram represents a less usual way of presenting phase relationships in solid state chemistry, but is sometimes used to express solubility information for two "binary" salts which have no common ion. Since such a diagram represents an intersection through the three-dimensional space filled with four-

or three-phase tetrahedral envelopes (which degenerate into a square when *two* parallel solid-solution ranges occur), spatial information is required for correct construction of the intersections with the multiphase walls of the envelopes. On the other hand, mole-balance considerations of phase contents can indicate relatively precisely where to look for new phases which surround the section. In the special case when two of the involved components are chemically similar, the square section provides a particularly convenient format for comparison of solid solubilities. This is the situation in the present system, whose significance consists mainly of the fact that it comprises three mutually closely related structures, of which only one so far is found to exhibit high-T_c superconductivity, viz., $YBa_2Cu_3O_7$.

Like $YBa_2Cu_3O_6$, the $YBa_2Fe_3O_8$ structure exhibits an antiferromagnetical ordering of the iron moments (*2*), but unlike $YBa_2Cu_3O_6$, the Néel temperature of $YBa_2Fe_3O_8$ is surprisingly high. (*21*). An electron or hole doping could then create a frustrated antiferromagnet state which precedes the transition into a metallic and superconducting state in certain cuprates. However, despite this, we do not expect superconductivity to occur for the doped $YBa_2Fe_3O_8$ phase. Otherwise, doped $YBa_2Fe_3O_8$ would provide a first example of a superconducting oxide where the central atom of the oxometallate anionic network does not possess the feature of an energetically separated (nondegenerated, single) orbital with fractional occupancy—a condition we have discussed in Ref. (*22*).

Acknowledgment

This work received financial support from the Norwegian Council for Science and the Humanities (NAVF).

References

1. G. Le Flem, G. Demazeau, and P. Hagenmuller, *J. Solid State Chem.* **44,** 82 (1982).
2. Q. Huang, P. Karen, V. L. Karen, A. Kjekshus, J. W. Lynn, A. D. Mighell, N. Rosov, and A. Santoro, *Phys. Rev. B: Condens. Matter* **45,** 9611 (1992).
3. P.-E. Werner, "Program SCANPI-6," Institute of Inorganic Chemistry, University of Stockholm, Sweden (1988).
4. P.-E. Werner, *Z. Kristallogr.* **120,** 375 (1964); "Version TREOR-5" (1988).
5. N. O. Ersson, Program CELLKANT, Chemical Institute Uppsala University, Uppsala, Sweden (1981).
6. J. Fiala, *Silikaty* **29,** 273 (1985).
7. P. H. Andresen, H. Fjellvåg, P. Karen, and A. Kjekshus, *Acta Chem. Scand.* **45,** 698 (1991).
8. A. R. Moodenbaugh, C. Y. Yang, Yimei Zhu, R. L. Sabatini, D. A. Fischer, Youwen Xu, and M. Suenaga, *Phys. Rev. B: Condens. Matter* **44,** 6991 (1991).
9. S. Katsuyama, Y. Ueda, and K. Kosuge, *Physica C (Amsterdam)* **165,** 404 (1990).
10. P. Karen, H. Fjellvåg, and A. Kjekshus, in preparation.
11. L. Er-Rakho, C. Michel, P. Lacorre, and B. Raveau, *J. Solid State Chem.* **73,** 531 (1988).
12. A. J. Jacobson, *Acta Crystallogr. B* **32,** 1087 (1976).
13. S. Meriani, *Acta Crystallogr. B* **28,** 1241 (1972).
14. S. Åsbrink and L.-J. Norrby, *Acta Crystallogr. B* **26,** 8 (1970).
15. W. Gutau and Hk. Müller-Buschbaum, *J. Less-Common Met.* **152,** L11 (1989).
16. B. D. Dunlap, J. D. Jorgensen, C. Segre, A. E. Dwight, J. L. Matykiewicz, H. Lee, W. Peng, and C. W. Kimball, *Physica C (Amsterdam)* **158,** 397 (1989).
17. M. Parras, E. Garcia, J. M. González Calbet, and M. Vallet-Regi, *J. Less-Common Met.* **169,** 25 (1991).
18. I. Halász, V. Fulop, I. Kirschner, and T. Porejsz, *J. Cryst. Growth* **91,** 444 (1988).
19. L. A. Klinkova, I. V. Soikina, and I. M. Romanenko, *Zh. Neorg. Khim.* **35,** 446 (1990).
20. T. Graf, J. L. Jorda, and J. Muller, *J. Less-Common Met.* **146,** 49 (1989).
21. P. Karen and A. Kjekshus, to be published.
22. P. Karen, H. Fjellvåg, and A. Kjekshus, *J. Solid State Chem.* **97,** 257 (1992).